Journal of Environmental Management 267 (2020) 110582

Contents lists available at ScienceDirect

Journal of Environmental Management

journal homepage: http://www.elsevier.com/locate/jenvman

Research article

# High temperature $Mn_2O_3/Mn_3O_4$ and $Co_3O_4/CoO$ systems for thermo-chemical energy storage

Jia Liu [a,b], Jan Baeyens [b], Yimin Deng [c], Xianlu Wang [d], Huili Zhang [a,*]

[a] College of Life Science and Technology, Beijing University of Chemical Technology, 15# Beisanhuan East Road, Chaoyang District, Beijing, 100029, PR China
[b] Beijing Advanced Innovation Center for Soft Matter Science and Engineering, Beijing University of Chemical Technology, 15# Beisanhuan East Road, Chaoyang District, Beijing, 100029, PR China
[c] Process and Environmental Technology Lab, Department of Chemical Engineering, KULeuven (KUL), J. De Nayerlaan 5, 2860, Sint-Katelijne-Waver, Belgium
[d] Hualu Engineering Technology Co., Ltd., Hualu Building, 7# Tangyan South Road, Yanta District, Xi'an, Shanxi, 710065, PR China

ARTICLE INFO

*Keywords:*
$Mn_2O_3$ and $Co_3O_4$
Ultrafine particles
BET surface Area and pore characteristics
Thermo-chemical energy storage
Reversible redox reaction
Kinetics
Reaction reversibility

ABSTRACT

A major action to reduce $CO_2$ emissions is replacing fossil fuels by renewable energy sources. Matching the energy supply and demand by the mostly intermittent renewable resources (wind, solar, wave) is hence a hot topic, and energy storage has become crucial. Thermo-chemical energy storage (TCES) has a higher energy density than sensible and latent heat storage, and allows energy to be stored in the reaction products for multiple reuse and even off-site application. Design parameters are the equilibrium temperature, the reaction heat and the reaction rate, as obtained from both thermodynamic and kinetic assessments. Equilibrium temperatures of the selected metal oxides, $Mn_2O_3/Mn_3O_4$ and $Co_3O_4/CoO$ are between 1115 K and 1179 K. The present research studies both redox reactions as examples. Commercial $Mn_2O_3$ and $Co_3O_4$ were previously investigated in detail, and suffer from incomplete reversibility. The present study investigates the use of self-made $Mn_2O_3$ and $Co_3O_4$ mesoporous particles, of micrometer or nanometer scale, respectively. The average particle size of self-made $Mn_2O_3$ particles is $< 5$ μm, with a BET surface area of 239.7 $m^2/g$, and $T_{eq}$ of 1177 K at ambient pressure. Self-made $Co_3O_4$ was of nano size, with average size of about 100 nm, a BET surface area of 54.2 $m^2/g$, and $T_{eq}$ of 1109 K at ambient pressure. The redox reactions of these ultrafine particles are fast and nearly fully reversible. The effect of adding inert $Al_2O_3$ or $Fe_2O_3$ was also studied, but proven to offer no kinetic benefit, while reducing the reaction heat due to their inert additive character. The findings were used in the design of a 10 kW TCES pilot plant that is currently being tested in a concentrated solar furnace.

## 1. Introduction

### 1.1. Thermal energy storage

The required reduction of $CO_2$ emissions will enhance the application of renewable energy sources in the fuel substitution and power generation. Since these renewable resources are mostly of intermittent nature (wind, solar, waves), matching energy supply and demand becomes a major concern. Especially in future power generation systems powered primarily by such renewable energy sources, it will be difficult to meet the stability requirements of the power network unless introducing energy capture and storage facilities, that will enhance the use of intermittent renewable energy and offer an economic alternative to grid expansion and load shedding.

Thermal energy storage (TES) systems can be screened by comparing the overall thermodynamic performance and chemical engineering properties including kinetics, design factors and thermal cycling. These factors ultimately determine their practicality, investment and operating costs. Latent heat storage (LHS) and thermo-chemical energy storage (TCES) broaden the development direction for TES. LHS uses phase change materials and has been widely studied in the range of 200–900 °C for latent heats between ~200 and 400 kJ/kg (Fernandes et al., 2012; Li et al., 2020; Naish et al., 2008; Zhang et al., 2017, 2016a). Chemical reaction enthalpy storage is applied in a TCES system, where the reaction enthalpy of the reversible thermo-chemical reactions (~200 kJ/kg to>1000 kJ/kg) adds up with the sensible heat (Angerer et al., 2018; Farcot et al., 2018; Hawwash et al., 2017; Liu et al., 2020, 2019; Tescari et al., 2014). If a compound with a specific heat capacity

* Corresponding author.
*E-mail address:* zhhl@mail.buct.edu.cn (H. Zhang).

https://doi.org/10.1016/j.jenvman.2020.110582
Received 11 March 2020; Received in revised form 5 April 2020; Accepted 6 April 2020
Available online 29 April 2020

of ~1 kJ/(kg·K) is used for heat storage at temperatures between 300 °C and 700 °C, the capacity of sensible heat storage (SHS) is 400 kJ/kg; between 500 and 800 kJ/kg in LHS due to the contribution of the heat of phase transition; and largely in excess of 1000 kJ/kg for TCES. The operating temperatures should be as high as possible in order to make better use of high energy storage densities. The thermo-chemical energy storage systems require the development and application of existing and/or new materials. The growing interest in TCES is demonstrated by the increasing number of publications, as illustrated in Fig. 1 showing that publications related to TCES research have more than tripled over the past 8 years. Within these publications, the use of ultrafine particles (micro- or nanoscale) was not reported before towards TCES applications, and is therefore a novel contribution of the present research. Ultrafine particles, mostly nanoparticles, were however reported for applications in SHS (to enhance the thermal conductivity and specific heat of the SHS carrier), or in LHS to improve the LHS material thermal conductivity and reduce the superheeating or cooling at the phase change temperature.

### 1.2. Principles of a TCES system

Thermo-chemical energy storage (TCES) utilizes a reversible chemical reaction to absorb and release heat. The amount of stored heat is proportional to the amount of storage material ($m$), the endothermic heat of the reaction ($\Delta H_r$) and the conversion ($\alpha \leq 1$), given as:

$$Q = m\alpha\Delta H_r \tag{1}$$

The total heat to be applied will exceed $\Delta H_r$ since the sensible heat of the reactants needs to be supplied between their initial (ambient) temperature and the reaction temperature. Different reversible chemical reactions can be applied, each reaction with its specific equilibrium temperature and reaction heat. Reaction pairs within the temperature range of 250–~900 °C (530–1180 K) are listed in Table 1, with thermodynamic data retrieved from NIST (Chase, 1988). It is clear that for high temperature TCES, only redox pairs with $T_{eq}$ exceeding 1100 K can be considered.

The equilibrium temperature, $T_{eq}$, is an important thermodynamic parameter for the preliminary evaluation and screening of reversible reaction systems, and can be obtained by applying the Gibbs free energy.

$$\Delta G(T_{eq}, P) = 0 \tag{2}$$

with $\Delta G$ as the Gibbs free energy change of the reaction, i.e. $\Delta G = \Delta H - T\Delta S$. $T_{eq}$ is hence defined by:

**Table 1**
Possible reversible reaction pairs (in decreasing order of $T_{eq}$).

| Reaction A ↔ B + C (+D) | $C_p$ (of A) kJ/(kg·K), at $T_{eq}$ | $T_{eq}$ at P = 1 atm, in K | $\Delta H_r$ at $T_{eq}$ [kJ/kg of A] |
|---|---|---|---|
| $6Mn_2O_3 \leftrightarrow 4Mn_3O_4 + O_2$ | 0.986 | 1177 | 185 |
| $2Co_3O_4 \leftrightarrow 6CoO + O_2$ | 0.231 | 1109 | 844 |
| $CaCO_3 \leftrightarrow CaO + CO_2$ | 1.052 | 1106 | 1703 |
| $CaMg(CO_3)_2 \leftrightarrow MgO + CaO + 2CO_2$ | 0.910 | 761 | 868 |
| $Ca(OH)_2 \leftrightarrow CaO + H_2O$ | 1.209 | 750 | 1288 |
| $MgCO_3 \leftrightarrow MgO + CO_2$ | 0.839 | 576 | 1126 |
| $Mg(OH)_2 \leftrightarrow MgO + H_2O$ | 1.306 | 532 | 1396 |

$$T_{eq} = \frac{\Delta H(T_{eq}, P)}{\Delta S(T_{eq}, P)} \tag{3}$$

with the reaction enthalpy $\Delta H$ and reaction entropy $\Delta S$ at pressure $P$ and temperature $T_{eq}$. The reaction entropy of the decomposition reaction is positive, and the reaction entropy of the reverse (recomposition) reaction is negative, but the absolute values of both are the same.

Fig. 2 illustrates calculated $T_{eq}$ results for the reaction pairs of Table 1. According to the partial pressure level, the figure can be divided into two regions. When the partial pressures of the gaseous or vapor reactants, $P$, are low, as is the case of applying TCES in an open system, the effect of the pressure $P$ on the equilibrium temperature $T_{eq}$ is very significant. The equilibrium temperature $T_{eq}$ is almost constant only when the partial pressure $P$ is high, except for $Mn_2O_3$ where a significant increase of equilibrium temperature $T_{eq}$ is calculated in a wide pressure range.

The reverse reactions with $O_2$/air are preferred since (i) the reverse reactions involving steam require the evaporation of $H_2O$, thus reducing the energy efficiency of the system; while (ii) the reactions involving $CO_2$ are the less obvious choice because the $CO_2$ produced by the decomposition reaction needs to be stored for later multiple use. Despite these inherent drawbacks, the focus of previous research was mostly on systems involving carbonate/oxide, and oxide/hydroxide systems. Contrary to carbonate/oxide and oxide/hydroxide systems, metal oxides do not call upon steam or $CO_2$. The reduction releases $O_2$, and the reversible re-oxidation can use air as driving reactant. Relevant previous publications for different metal oxide pairs were summarized in Supplementary Information, Tables SI–1, however with a main focus on $Co_3O_4$/CoO and $Mn_2O_3$/$Mn_3O_4$ systems. The $Co_3O_4$/CoO transition can be nearly complete (Agrafiotis et al., 2015a, 2015b; Alonso et al., 2016; Block and Schmücker, 2016) with a potential application for TCES

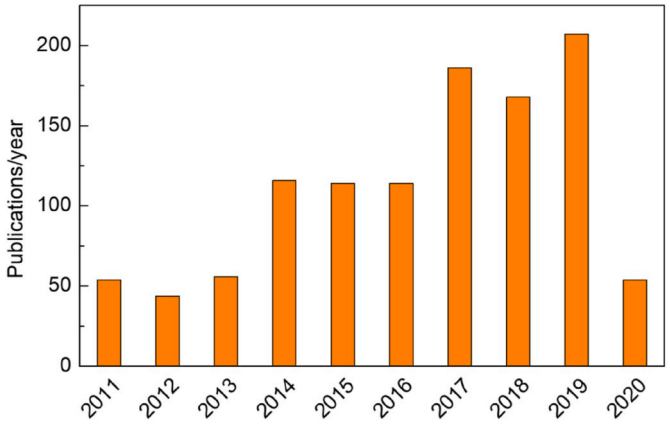


**Fig. 1.** The growing research interest in TCES: number of publications/year (till March 01, 2020). From Scopus with keywords thermo-chemical, energy, storage. (28.3% conference papers; 62.0% articles; 6.5% reviews; 3.2% book chapters).

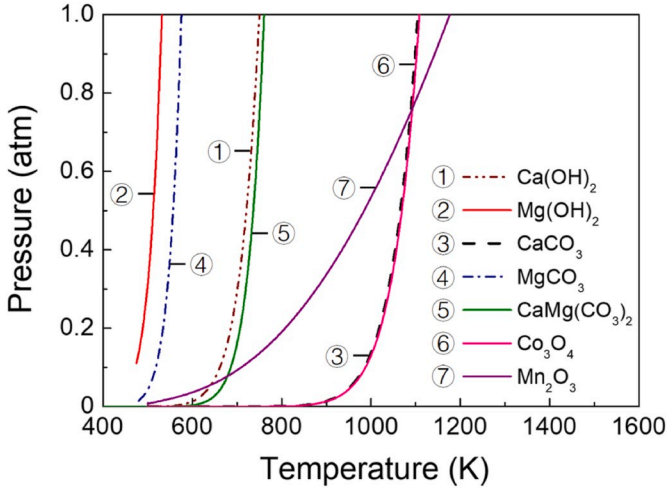


**Fig. 2.** Equilibrium temperature versus pressure for selected reaction pairs (Zhang et al., 2016d, 2016a).

around 900 °C (Silakhori et al., 2019; Zhang et al., 2016a, 2016b, 2016c, 2016d). Denser $Co_3O_4$-pellets could not maintain their structural integrity, showing cracks after only two cycles. Foams were tested for 15 redox cycles, maintaining their structural integrity and stoichiometric redox performance (Agrafiotis et al., 2015b). Honeycombs from pure cobalt oxide and cobalt oxide-coated cordierites exhibited a similar redox performance. The addition of alumina has a negative effect on the redox performance but significantly increases the honeycombs structural stability (Pagkoura et al., 2015). Iron-doped cobalt-oxides transform at a similar temperature as pure cobalt-oxide (915 °C). The reaction enthalpy gradually decreases with increasing iron content. Compositions of 10% iron-oxide exhibit the most outstanding properties, and the reversibility of the reduction reaction and re-oxidation is superior than in pure $Co_3O_4$ (Block et al., 2014).

$Mn_2O_3/Mn_3O_4$ has also been studied as commercial compounds (Bielsa et al., 2019), but mostly when mixed with other metal oxides to improve the recyclability e.g. (Agrafiotis et al., 2017; Al-Shankiti et al., 2019; André et al., 2017; André and Abanades, 2017; Gokon et al., 2019). In general, both $Co_3O_4$ and $Mn_2O_3$ suffer from consolidation of the reduced CoO and $Mn_3O_4$ respectively, thus hampering the reverse reactions, while doping narrows the thermal hysteresis loop, thus improving energy storage efficiency and cycle stability (Carrillo et al., 2016, 2015), the number of achievable redox cycles remains low, with a maximum of 100 cycles reported (Wokon et al., 2017a, 2017b).

In view of the unsatisfactory results previously reported towards the use of commercial $Mn_2O_3$ and $Co_3O_4$, the present study focuses upon the application of self-made ultrafine $Mn_2O_3$ and $Co_3O_4$, however in comparison with their commercially available equivalents, to investigate and explain previously mentioned shortcomings of incomplete reversibility.

The paper therefore.

(i) experimentally investigates the target metal oxide TCES materials. Both the reference commercial and self-made oxides will be tested and compared. The possible role of inert additives ($Al_2O_3$ and $Fe_2O_3$) was also investigated to determine their possible role in enhancing the reactions;
(ii) transform the experimental TGA results into reaction kinetics;
(iii) apply the thermodynamic and kinetic data, by way of example, in the design of pilot 10 kW TCES storage module, currently further evaluated in a concentrated solar heat storage module.

## 2. Experimental methods and materials

### 2.1. Generalities

The redox pairs $Mn_2O_3/Mn_3O_4$ and $Co_3O_4$/CoO were selected for in-depth analysis. Not only the data at thermodynamic equilibrium are important, but both the kinetics, i.e. the rates of progress of the forward and backward reaction, and the cycling performance need to be considered since they must be compatible with the required TCES charging/discharging duties.

With thermo-gravimetric analysis, the extent of the reduction and oxidation can be determined, even in cycling experiments. The rates of reduction/oxidation moreover determine the kinetic constants of the different reactions. A Thermo-gravimetric Analyser of Mettler Toledo STARe system TGA/DSC3+ was used at atmospheric pressure with a nitrogen flow of 50 mL/min for the reduction reactions. For the selected reaction pairs, the reverse oxidation reactions were studied in air (50 mL/min). As recommended by several previous studies (Brems et al., 2011; Pan and Zhao, 2017; Van de Velden et al., 2010), and considering the required degree of conversion (≥98%), the reaction heat, and the specific heat capacity, a temperature ramp (heating ramp, $\beta$, in K/min) of 20 K/min was used for the experiments and all experiments were repeated three times. The average results are reported with a standard deviation between individual results and the averages of maximum 5%. The TGA reduction experiments result in a plot of the weight loss in function of the temperature, and hence time, in view of the fixed temperature ramp ($\beta$, in K/min). For the reverse oxidation reaction involving $O_2$ (air), a similar procedure was used, although in this case, a weight gain is recorded with time progressing. The DSC part of the Mettler Toledo STARe system TGA/DSC3+ was not further reported, since results confirmed the literature reaction heats within ± 2%. Also, the reaction heat when adding inert substance was reduced in proportion to the real amount of redox reactant present.

### 2.2. Commercial, self-made and Al-doped $Mn_2O_3$

Both commercial $Mn_2O_3$ (Aladdin Industrial Corporation, China) and self-prepared $Mn_2O_3$ were used. Self-made $Mn_2O_3$ was prepared by precipitation of $Mn^{2+}$ from $MnSO_4{\cdot}H_2O$ (Sinopharm Chemical Reagent Co., Ltd., China) by oxalic acid (Shanghai Yuanye Biotechnology Co., Ltd., China). $NH_4OH$ (Beijing Chemical Factory, China) was added to adjust the pH of the reaction solution into a weakly acidic range. The $MnC_2O_4$ was thereafter calcined in a furnace at 400 °C for 3 h according to the methods of Zhou et al. (2013), and black $Mn_2O_3$ was obtained.

$$4MnC_2O_4{\cdot}2H_2O + 3O_2 \xrightarrow{400^\circ C} 2Mn_2O_3 + 8CO_2 + 8H_2O \quad (4)$$

For the synthesis of mixed Mn–Al-oxides, a similar process was repeated with $MnSO_4{\cdot}H_2O$ and $Al_2(SO_4)_3{\cdot}18H_2O$ (Sinopharm Chemical Reagent Co., Ltd., China) in the appropriate weight ratio: $Al_2(SO_4)_3$ was added to the $MnSO_4$ solution in such a weight ratio as to obtain the mixed precipitate of Mn–Al-oxalate at the desired wt%. The mixed precipitate of Mn–Al-oxalate was calcined at 400 °C of 3 h to obtain the mixed oxide at the selected 9.5 or 18.2% wt% of $Al_2O_3$ in the mixed Mn–Al-oxide. It was experimentally confirmed that the production of a fully intercrystalline mixed oxide required a slow calcination rate (≤2 K/min). The surface morphology of the samples was characterized by JEOL JSM-7800 F field emission scanning electron microscope (FESEM). Commercial $Mn_2O_3$, self-made $Mn_2O_3$ and Al-doped $Mn_2O_3$ (9.5 and 18.2% Al) have completely different particulate morphology, as illustrated in SEM-imaging of Fig. 3-a/b/c/d.

It can be seen from Fig. 3-a that the commercial $Mn_2O_3$ particles are mostly irregular particles. The self-made $Mn_2O_3$, Al-doped $Mn_2O_3$ (9.5% Al) and Al-doped $Mn_2O_3$ (18.2% Al) are all layered particles, and the surface of the particles becomes increasingly dense as the doping amount of Al increases. Self-made $Mn_2O_3$ particles have an average particle size <5 μm. Commercial $Mn_2O_3$ particles are of a broader particle size, but on average ≪ 3 μm, as determined by Malvern laser diffraction. This particle morphology will also affect the BET-results as shown hereafter.

The exclusive presence of $Mn_2O_3$ was determined by XRD measurement, as illustrated in Fig. 4. During the preparation of $Mn_2O_3$, $MnC_2O_4{\cdot}2H_2O$ and $MnC_2O_4$ completely decomposed completely at temperatures below the calcination temperature of 400 °C. Only the characteristic peaks of $Mn_2O_3$ are shown in the XRD of the self-made $Mn_2O_3$, hence $MnO_2$ and oxalates did not occur.

### 2.3. Commercial $Co_3O_4$ and self-made $Co_3O_4$

According to the methods of Wei et al. (2015), $Co_3O_4$ nanoparticles were synthesized by dropwise adding 500 mL of aqueous solution containing 0.934 g of $Co(CH_3COO)_2{\cdot}4H_2O$ (J&K Scientific) to 500 mL of aqueous solution containing 0.830 g of $K_3$ $[Co(CN)_6]$ (J&K Scientific) and 15 g of polyvinylpyrrolidone K30 (Tokyo Chemical Industry Company) by utilizing a syringe pump. The reaction solution was left to stand. It was aged for 24 h after being stirred for 30 min at room temperature. The sediment $Co_3$ $[Co(CN)_6]_2{\cdot}nH_2O$ was collected by centrifugation and washed with high purity water for three times and then dried in the oven at 65 °C for 12 h. Finally, the particulate $Co_3$ $[Co(CN)_6]_2{\cdot}nH_2O$ was calcined in air at 450 °C for 2 h with the heating rate

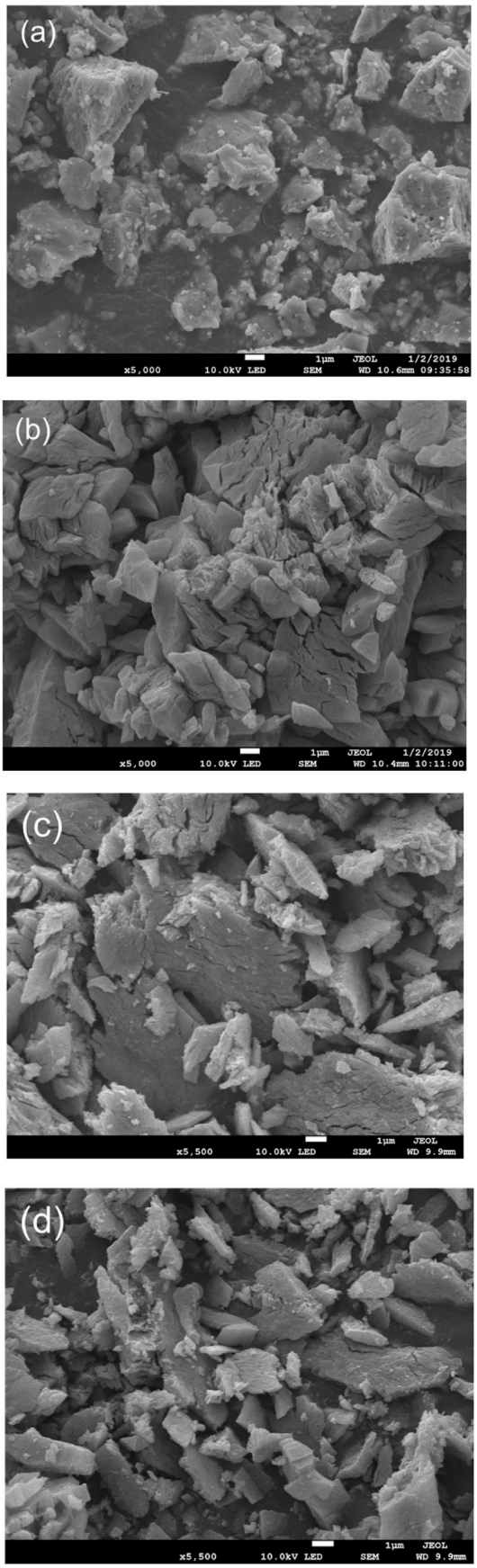


**Fig. 3.** SEM-imaging of (a) commercial $Mn_2O_3$, (b) self-made $Mn_2O_3$, (c) Al-doped $Mn_2O_3$ (9.5% Al) and (d) Al-doped $Mn_2O_3$ (18.2% Al).

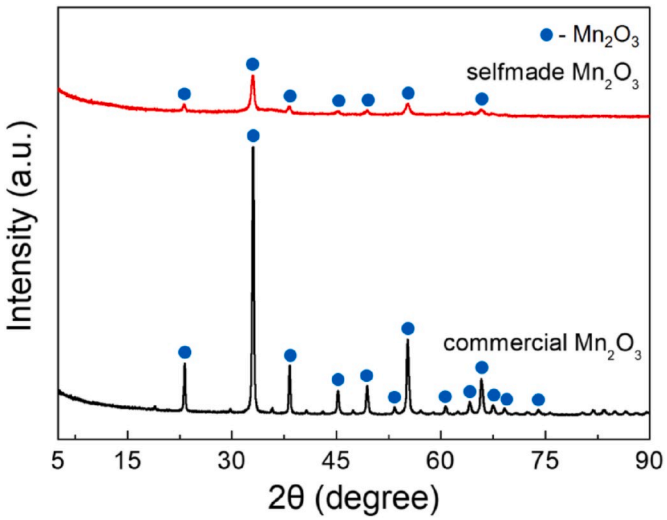


**Fig. 4.** XRD data of (a) commercial $Mn_2O_3$ and (b) self-made $Mn_2O_3$.

of 1 °C/min to obtain $Co_3O_4$ nanoparticles.

$$3Co(CH_3COO)_2{\cdot}4H_2O + 2K_3\left[Co(CN)_6\right] \rightarrow Co_3\left[Co(CN)_6\right]_2{\cdot}nH_2O + 6CH_3COOK + (12-n)H_2O$$

$$3Co_3\left[Co(CN)_6\right]_2{\cdot}nH_2O + 82O_2 \xrightarrow{450^{\circ}C} 5Co_3O_4 + 36CO_2 + 36NO_2 + 3nH_2O$$

Both commercial $Co_3O_4$ (Aladdin Industrial Corporation, China) and self-made $Co_3O_4$ have a completely different particulate structure, as illustrated in SEM-imaging of Fig. 5-a/b.

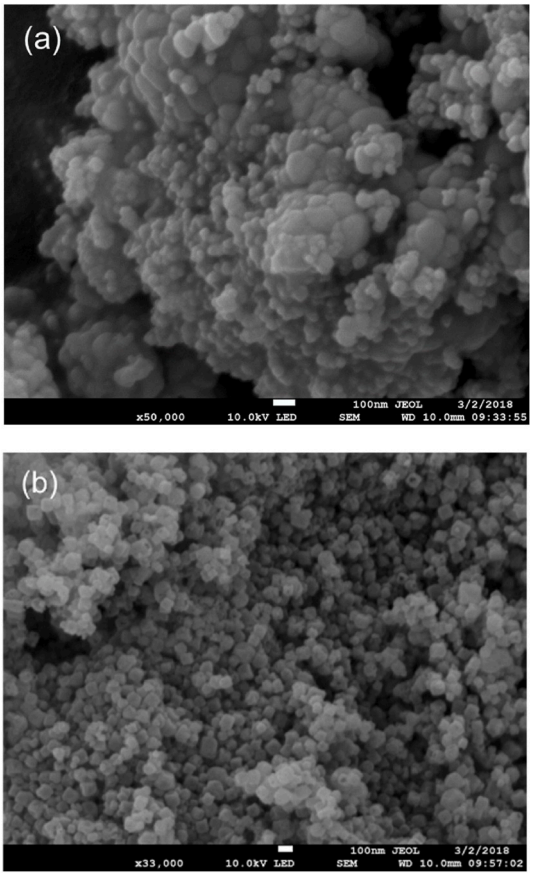


**Fig. 5.** SEM-imaging of (a) commercial $Co_3O_4$ and (b) self-made $Co_3O_4$.

The morphology of self-made $Co_3O_4$ nanoparticles is cubical, while the morphology of commercial $Co_3O_4$ particles is irregular. The self-made $Co_3O_4$ nanoparticles are uniform in size and have a particle size of about 100 nm. The size of the commercial $Co_3O_4$ particles has a size distribution from about 50 nm to 150 nm.

## 3. Results and discussion

### 3.1. Commercial and self-made $Mn_2O_3$

#### 3.1.1. TGA-results and discussion of the $Mn_2O_3/Mn_3O_4$ pair

The different samples were subjected to TGA experiments. The $Mn_2O_3$–$Mn_3O_4$ conversion is fast, and weight loss versus time is almost linear. The reverse $Mn_3O_4$– $Mn_2O_3$ is slower and occurs at lower temperatures (≥650 °C). Results are illustrated in Fig. 6-a/b. $T_{eq}$ is around 820–840 °C, slightly lower that the value indicated by the thermodynamic calculations of Table 1. The theoretical weight loss of $Mn_2O_3$ to $Mn_3O_4$ is 3.38%. The figure shows that this theoretical value is on average achieved. The figure also illustrates that a cyclic operation for 5 redox-cycles achieves a high efficiency with the initial weight of $Mn_2O_3$ nearly re-established for the ultrafine $Mn_2O_3$ (Fig. 6-b), but with a lesser degree of weight restitution for the commercial product.

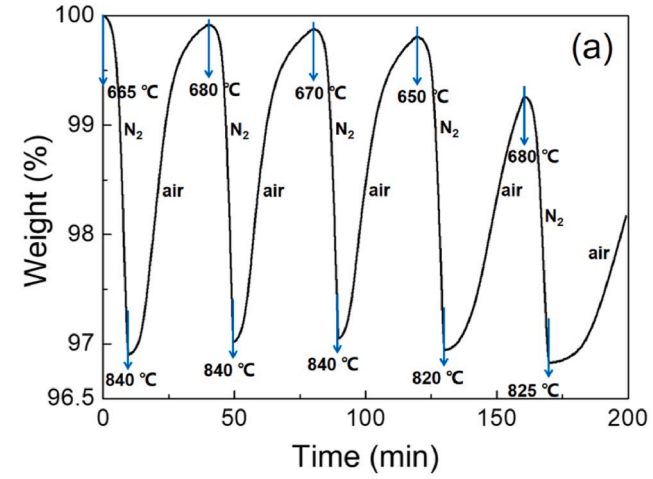


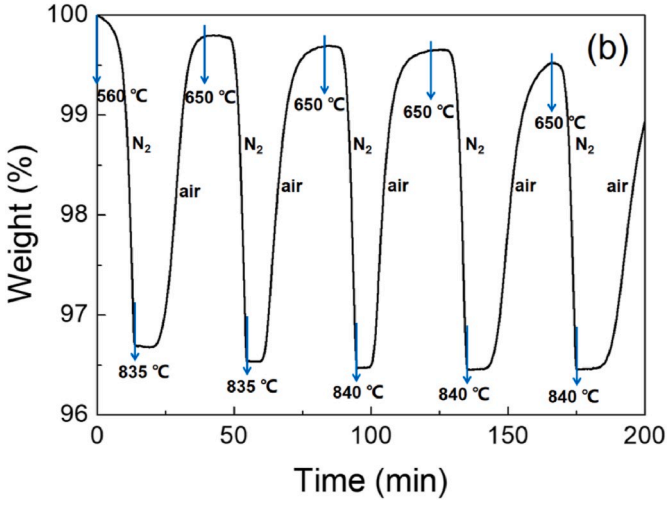


**Fig. 6.** TGA results at β = 20 °C/min of (a) commercial $Mn_2O_3$ and (b) self-made $Mn_2O_3$, for 5 cycles within 200 min. The temperature was first increased to 840 °C in $N_2$, then the gas was switched to air, and the temperature was maintained at 650 °C for 20 min.

The effect of Al-doping is limited, although its inclusion in the $Mn_2O_3$ crystal reduces the endothermic heat per gram unit weight. Illustration of the limited effect is given in Fig. 7, limited to 2 cycles. The weight recovery after re-oxidation is lower than in the pure $Mn_2O_3$ systems of Fig. 6-a/b.

Similar results were obtained when adding $Fe_2O_3$ into self-made $Mn_2O_3$, prepared according to the equivalent method of co-precipitation but with $FeSO_4$, followed by mild calcination. Adding 5–10 wt% $Fe_2O_3$ appears to facilitate the a fair degree of $Mn_2O_3$ recovery after re-oxidation.

#### 3.1.2. BET-results and discussion

Nitrogen adsorption–desorption isotherms were measured using a Micromeritics ASAP 2020. The BET analysis was performed for all $Mn_2O_3$ samples, as summarized in Table 2, together with the results of Al-doped $Mn_2O_3$. The BET specific surface area decreases during the forward reaction due to the consolidated structure of $Mn_3O_4$ with lower porosity. The pore volume of $Mn_2O_3$ and Al-doped $Mn_2O_3$ (9.5% Al and 18.2% Al) decrease after the reduction process, but increase after re-oxidation reaction, which demonstrates their good cyclic performance. Pores remain of mesoporous nature. Only for the self-made ultrafine particles, BET-values decrease in the reduction stage, but progressively increase again in the subsequent re-oxidation stages. These ultrafine particles hence offer a better potential for the reverse reaction than their commercial equivalent. This was already demonstrated from TGA results in Fig. 6. The addition (doping) by inert oxides does not significantly improve the results, despite the larger pore sizes obtained and hence contradicts earlier experiments where Al-doping was proposed to enhance the re-oxidation step (Tescari et al., 2014).

### 3.2. Commercial and NP $Co_3O_4$

#### 3.2.1. TGA-results and discussion of the $Co_3O_4/CoO$ pair

TGA testing was performed on the commercial $Co_3O_4$ particles and the self-made $Co_3O_4$ nanoparticles. The reaction of $Co_3O_4$ to CoO has a relatively fast conversion rate and its weight loss with respect to time is almost linear. The conversion rate of the reverse reaction of CoO–$Co_3O_4$ is slower. The results are shown in Fig. 8-a/b. The initial weight loss of the self-made $Co_3O_4$ nanoparticles during the heating period is due to the presence of a small amount of impurities in the product. $T_{eq}$ is approximately 900 °C and is consistent with the thermodynamic calculations. The theoretical weight loss of $Co_3O_4$ to CoO is 6.65 wt%. The

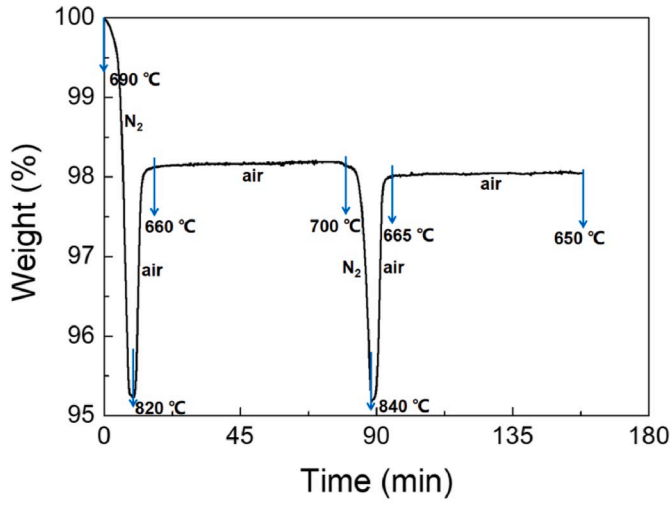


**Fig. 7.** TGA results at β = 20 °C/min of Al-doped $Mn_2O_3$ (9.5% Al), for 2 cycles within 160 min. The temperature was first increased to 840 °C in $N_2$, then the gas was switched to air, and the temperature was maintained at 650 °C for 60 min in air.

**Table 2**
History of BET and pore properties through the reaction cycles.

| Component | Property | | |
|---|---|---|---|
| | Pore volume ($cm^3/g$) | BET surface area ($m^2/g$) | Type of porosity & Pore width |
| Commercial $Mn_2O_3$ | | | |
| initial | 0.169 | 195.7 | Mesoporous (4.0 nm) |
| after reduction | 0.009 | 9.1 | Mesoporous (3.1 nm) |
| after re-oxidation | 0.017 | 16.4 | Mesoporous (3.4 nm) |
| after 2 cycles | 0.011 | 11.0 | Mesoporous (3.4 nm) |
| Self-made $Mn_2O_3$ | | | |
| initial | 0.284 | 239.7 | Mesoporous (2.7 nm) |
| after reduction | 0.054 | 34.3 | Mesoporous (5.4 nm) |
| after re-oxidation | 0.081 | 86.5 | Mesoporous (3.4 nm) |
| Al-doped $Mn_2O_3$ (9.5% Al) | | | |
| initial | 0.274 | 83.6 | Mesoporous (21.7 nm) |
| after reduction | 0.064 | 27.6 | Mesoporous (9.3 nm) |
| after re-oxidation | 0.182 | 86.4 | Mesoporous (10.9 nm) |
| after 2 cycles | 0.129 | 50.8 | Mesoporous (7.4 nm) |
| Al-doped $Mn_2O_3$ (18.2% Al) | | | |
| initial | 0.261 | 101.6 | Mesoporous (9.3 nm) |
| after reduction | 0.043 | 24.2 | Mesoporous (8.6 nm) |
| after re-oxidation | 0.060 | 57.3 | Mesoporous (3.4 nm) |

actual weight loss of the commercial and self-made $Co_3O_4$ is close to the theoretical value (~6.5 wt%). Both the commercial and self-made $Co_3O_4$ particles can complete a redox cycle with an efficiency of nearly 100% after a fairly long re-oxidation period.

### 3.2.2. BET-results and discussion

The BET analysis of the commercial $Co_3O_4$ particles and self-made $Co_3O_4$ nanoparticles are shown in Table 3. The BET specific surface area and pore volume of the commercial $Co_3O_4$ particles and self-made $Co_3O_4$ nanoparticles decrease during the reduction reaction, and the structure of commercial and self-made $Co_3O_4$ has a pronounced collapse. The very low BET-values confirm a crystal structure consolidation (also called sintering), and this phenomenon explains the long contact time required for the re-oxidation stage (Fig. 8). The pore volume and pore size of $Co_3O_4$ significantly decrease after the reduction reaction, hence reduce the reaction rate of the re-oxidation reaction with air to a certain extent, but it does not have a significant impact on the cycle performance, as shown in Fig. 8.

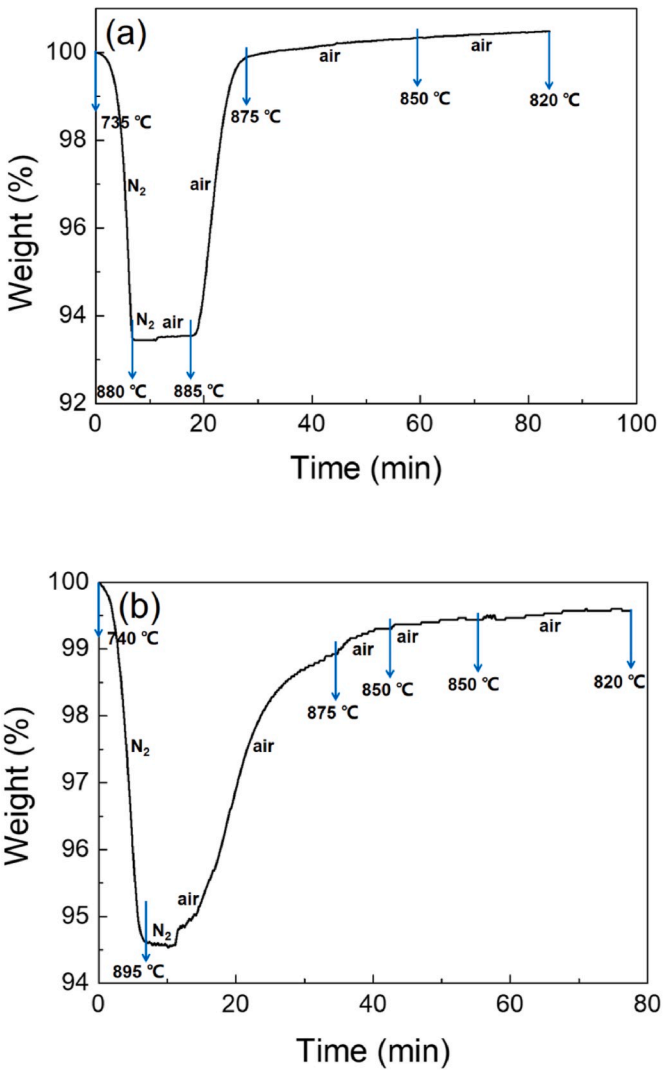


**Fig. 8.** TGA results at β = 20 °C/min of (a) commercial $Co_3O_4$ and (b) self-made $Co_3O_4$, for 1 cycle within 90 min. The temperature was first increased to 950 °C in $N_2$. the re-oxidation was maintained at 875 °C for nearly 50 min in air. Re-oxidation is hence a slow process.

### 3.3. Kinetic parameters

For the reduction reaction, the value of α is derived from the corresponding weight loss curve by equation (5):

$$\alpha = (m_0 - m) / (m_0 - m_f) \quad (5)$$

with $m_0$, m and $m_f$ are the initial mass of the sample, the mass at a given time t, and the final sample mass, respectively.

The Arrhenius expression can be used to relate the kinetic reaction constant, k with kinetic parameters E (activation energy) and A (pre-exponential constant):

$$k = A \exp(-E / RT) \quad (6)$$

To determine reaction kinetics from the TGA experiments, literature presented several methods (Brems et al., 2011; Fernandez et al., 2019; Mahmoudi et al., 2012; Van de Velden et al., 2010):

$$d\alpha / dt = k(T) f(\alpha) \quad (7)$$

where α is the degree of conversion, and f(α) is a function describing the reaction rate resistances.

**Table 3**
History of BET and pore properties through reaction cycle.

| Component | Property | | |
|---|---|---|---|
| | Pore volume ($cm^3/g$) | BET surface area ($m^2/g$) | Type of porosity & Pore width |
| Commercial $Co_3O_4$ | | | |
| Initial | 0.152 | 14.5 | Mesoporous (31.9 nm) |
| after reduction | 0.002 | 0.9 | Mesoporous (3.4 nm) |
| after re-oxidation | 0.003 | 1.1 | Mesoporous (3.4 nm) |
| Self-made $Co_3O_4$ | | | |
| initial | 0.245 | 54.2 | Mesoporous (25.7 nm) |
| after reduction | 0.001 | 0.2 | Mesoporous (4.2 nm) |
| after re-oxidation | 0.003 | 0.3 | Mesoporous (5.7 nm) |

Several expressions for g(α) are proposed in literature to account for the concepts of diffusion, nucleation and the order of the reaction, and applicable to different reactions: coarse biomass (diffusion), plastic solid waste (reaction order), lignin (mostly nucleation). For chemical

reactions, and certainly when using a small particle size of the solid raw material, as is the case in the present research, the reaction mechanism is generally first order reaction rate controlled, thus eliminating diffusion and nucleation models for further consideration as was demonstrated by Van de Velden et al. (Van de Velden et al., 2010) and Brems et al. (2011). The resulting first order conversion is simplified to:

$$\ln(1-\alpha) = -kt = -A\exp\left(\frac{E}{RT}\right)t \quad (8)$$

The redox reactions can indeed be fitted by a first order reaction rate between the temperature limits of the application, i.e. 1010–1129 K for $Mn_2O_3$ reduction, and 850–950 K for the $Mn_3O_4$ re-oxidation, where lnk is a linear function of 1/T.

The respective values of the Arrhenius equation are E = 265,200 J/mol and A = 6.58 × $10^9$ $s^{-1}$ for $Mn_2O_3$ reduction, and E = 279,000 J/mol and A = 7.08 × $10^9$ $s^{-1}$ for $Mn_3O_4$ re-oxidation in air. Applied to 1150 K for $Mn_2O_3$, these Arrhenius parameters imply a reaction rate constant, k, of 1.672 × $10^{-3}$ $s^{-1}$, meaning that a reduction of 98% will require a reaction time of 2344 s. Applied at 1100 K for $Mn_3O_4$ re-oxidation, this provides a k value of 4.02 × $10^{-4}$ $s^{-1}$. Re-oxidation at 98% will hence require a time of 9731 s: the re-oxidation is about 3 times slower than the reduction, as can also be seen in the TGA results.

For $Co_3O_4$, the respective values of the Arrhenius equation are E = 518,200 J/mol and A = 1.41 × $10^{21}$ $s^{-1}$ for $Co_3O_4$ reduction, and E = 526,300 J/mol and A = 2.46 × $10^{21}$ $s^{-1}$ for CoO re-oxidation in air. Applied to 1160 K for $Co_3O_4$, these Arrhenius parameters imply a reaction rate constant, k, of 6.53 × $10^{-3}$ $s^{-1}$, meaning that a reduction of 98% will require a reaction time of 599 s. Applied at 1160 K for CoO re-oxidation, this provides a k value of 4.92 × $10^{-3}$ $s^{-1}$. Re-oxidation at 98% will hence require a time of 795 s. Of course, a longer contact time will be required for a higher degree of conversion.

### 3.4. Final recommendations

TCES is of growing research and practical importance. Thermodynamic principles determine the equilibrium temperature and the heat of reaction. From the assessment, it is clear that the reaction pair $Co_3O_4$/CoO has major advantages in comparison with the $Mn_2O_3$/$Mn_3O_4$ reaction pair: its equilibrium temperature is 1109 K (against 1177 K for $Mn_2O_3$), its heat of reaction is 844 kJ/kg $Co_3O_4$ (against 185 kJ/kg $Mn_2O_3$ only). For a required TCES capacity, the amount of $Mn_2O_3$ will hence be about 4.6 times higher due to the lower heat of reaction.

Since both manganese and cobalt oxide can be produced as ultrafine particles (micro- or nanometer scale, respectively, high rates of reaction are obtained. The ultrafine particle size however requires specific gas/solid contacting modes i.e. using fixed or moving bed reactors, either at low gas velocities to avoid particle entrainment (Ranjha et al., 2017; Schmidt et al., 2016; Wokon et al., 2017b) and/or gas-channeling, or at higher velocities if the metal oxides are compressed to form porous pellets, or are deposited on inert carriers such as honeycombs (Fopah--Lele et al., 2016; Pagkoura et al., 2015) or coated ceramic structures (Agrafiotis et al., 2017, 2015a; 2015b). Alternatively, fluidized bed reactors can be used, although special designs are required to deal with the cohesive nature of the powders (Criado et al., 2017; Li et al., 2019; Rougé et al., 2017; Sabatier et al., 2020; Tregambi et al., 2017; Zhang et al., 2019). In our research, two methods were applied to ensure the particle fluidization, including vibrating the reactor containing the ultrafine particles (50 Hz with amplitude of 4 mm), and adding Degussa Aerosil® powder to reduce the cohesive Van der Waals forces between adjacent particles.

Due to the high reaction enthalpy and an equilibrium temperature of around 840 °C at atmospheric pressure, the $Co_3O_4$/CoO system is most suitable for high temperature thermal energy storage, as experienced in concentrated solar tower (SPT) applications (AuYeung and Kreider, 2017; Lei et al., 2017; Peng et al., 2017; Zhang et al., 2017, 2016c). Moreover, the storage material can be prepared in nanoparticle size at a fair cost (in fact low considering the multiple cycles of reuse). It can be processed with appropriate technologies with only minor safety hazards.

Taking the operating temperature into account, and to avoid excessive sensible heat losses by using gaseous heat transfer fluids in an open system, the concept of indirect solar heat capture by reduction and separate but subsequent heat recovery through oxidation can be adopted.

The tentative layout of this a system is represented in Fig. 9, and is currently tested in the 20 kW concentrated solar furnace operated by our research group (Fig. 10).

Fig. 10 illustrates the overall layout of the concentrated solar furnace. The fluidized bed receiver/reduction reactor is positioned in the cavity of the furnace. Heliostat and parabola are the concentrating elements of the rig.

With the normally experienced DNI values at the Qinhuangdao site (0.7–1.0 kW/$m^2$) and a heliostat surface area of 26 $m^2$, the collected solar capacity approaches 20 kW. Due to optical and thermal losses, only ~50% is recorded at the cavity itself, hence having a maximum thermal capacity of ~10 kW.

As shown in Fig. 9, the reactor will be emptied via a raceway vibrating L-valve into an insulated hot storage hopper when the equilibrium temperature is attained, and the residence time is deemed sufficient according to the previously determined kinetics (at least 15 min at ~840 °C) (Smolders and Baeyens, 1995).

The re-oxidation stage is carried out in a shallow bubbling fluidized bed and re-oxidized $Mn_2O_3$ is recycled to the hot feeding storage. Heat recovery from the shallow fluidized bed can be performed as compressed air and a Brayton cycle turbine, or further used in a steam boiler and applied in a steam engine/turbine) (Kang et al., 2018; Sabatier et al., 2020). Alternatively, the hot particles can be used as heat supply medium to the hot-side heat exchanger of a Stirling electricity generation (Zhang et al., 2016c).

Due to the very fine nature of the reactants, and the vibration-aided fluidization, superficial gas velocities (either $N_2$ in reduction stage, or air in re-oxidation) are very low (≪ 1 cm/s), thus limiting sensible heat losses, attrition (Zhang et al., 2016b) and equipment erosion (Van de Velden and Baeyens, 2007).

The use of sintered metal or ceramic fiber filters (Schildermans et al., 2004; Smolders and Baeyens, 2000) moreover makes gas recycling and/or heat recovery possible. A 10 kW heat capture/storage capacity, to be achieved in e.g. 1 h, requires an amount of $Co_3O_4$ equal to 43 kg (for $Co_3O_4$ cycling from 750 °C to 850 °C and $\Delta H_R$ = 844 kJ/kg). With a bulk density of 2590 kg/$m^3$, the receiver-reactor needs to contain 17 L of bulk powder. Its internal diameter is 0.25 m for a bed height of 0.33 m (total reactor height: 0.4 m).

If $Mn_2O_3$ were used for the same application, its significantly lower reaction heat ($\Delta H_R$ = 185 kJ/kg) will increase the amount of TCES material required, despite its higher specific heat capacity (0.986 against 0.231 kJ/(kg·K) for $Co_3O_4$). With a bulk density of nearly 3000 kg/$m^3$, the receiver-reactor will need to contain about 60 L of bulk powder. Its internal diameter should then preferably be increased to 0.40 m for a bed height of 0.43 m (total reactor height: 0.5 m).

Full details of the pilot operations will be presented in a follow-up paper.

## 4. Conclusions

A large number of reversible chemical reactions can be used for thermo-chemical energy storage, each with a given range of equilibrium temperatures and heats of reaction. Redox pairs with high reaction heats are not necessarily the most interesting ones from an energy storage and re-use point of view, due to the required reactant for the reverse reaction ($O_2$/air easier that steam and $CO_2$). TGA experiments determine the reaction time required.

Both self-made $Mn_2O_3$ and $Co_3O_4$ have good reversibility in multiple

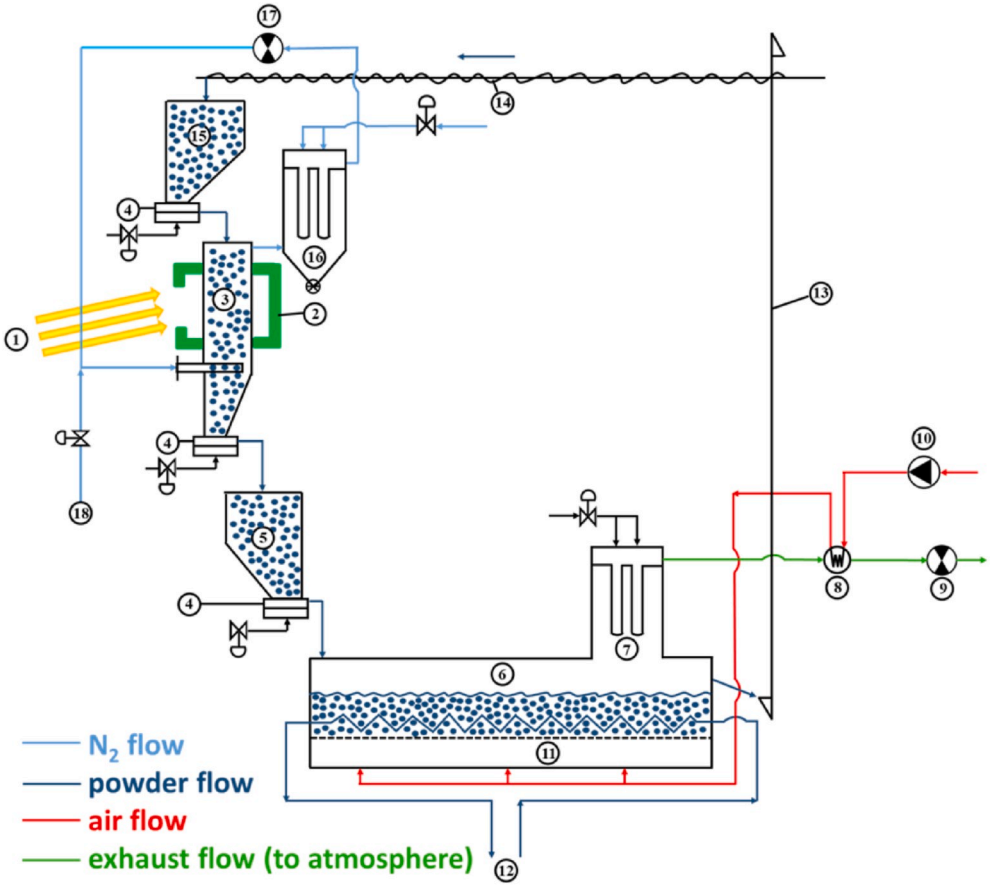


**Fig. 9.** Layout of the integrated solar-heated TCES pilot plant, with: ① Heliostats; ② Insulated cavity; ③ Receiver-TCES reduction step; with tubular multi-orifice distributor; ④ Raceway vibrating discharge valve; ⑤ Hot storage hopper; ⑥ Fluidized bed TCES re-oxidation step; ⑦ Pulse get cleaned (air) sintered metal fiber filter; ⑧ Heat exchanger; ⑨ Exhaust fan; ⑩ Air blower; ⑪ Air distribution; ⑫ To/from power block; ⑬ Bucket elevator; ⑭ Screw conveyor; ⑮ Feeding hopper; ⑯ Pulse get cleaned ($N_2$) sintered metal fiber filter; ⑰ $N_2$ recycle fan; ⑱$N_2$ back-up feed.

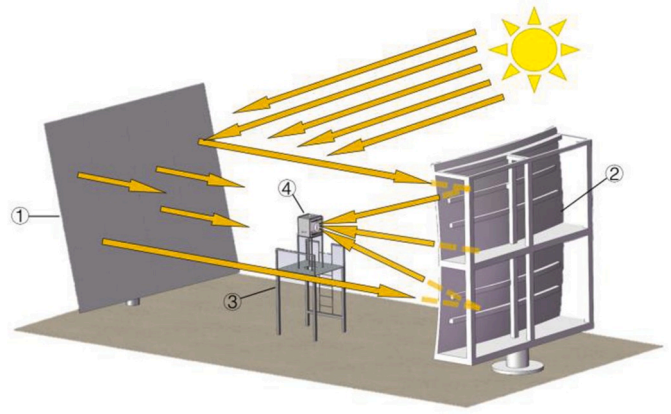


**Fig. 10.** Experimental solar furnace layout, with: ①Sun-tracking heliostat; ②Concentrating parabola; ③Support structure of solar furnace; ④Experimental solar cavity, with 0.3 m I.D. aperture.

cycle reactions. For self-made $Mn_2O_3$, the BET surface area is 239.7 $m^2$/g, with pore width of 2.7 nm, and pore volume of 0.284 $cm^3$/g. For self-made $Co_3O_4$, the BET surface area is 54.2 $m^2$/g, with pore width of 25.7 nm, and pore volume is 0.245 $cm^3$/g. SEM analyses and BET confirm that the reduction products of $Mn_3O_4$ and CoO have a denser morphology, but do only slightly reduce the efficiency of the re-oxidation reaction, and this for multiple cycles. Doping $Mn_2O_3$ with inert oxides has no significant advantages.

The analysis of the reaction kinetics demonstrate that the reduction reaction of $Mn_2O_3$ is about 3 times faster than the re-oxidation reaction, as can also be seen in the TGA results. For $Co_3O_4$, the reduction and re-oxidation reactions are nearly equally fast, but significantly faster than the $Mn_2O_3/Mn_3O_4$ pair.

Finally, the strategy behind and the design of a 10 $kW_{th}$ TCES pilot unit is described.

## Declaration of competing interest

There are no conflicts to declare.

## CRediT authorship contribution statement

**Jia Liu:** Conceptualization, Data curation, Formal analysis, Investigation, Validation, Visualization, Writing - original draft, Writing - review & editing. **Jan Baeyens:** Conceptualization, Funding acquisition, Methodology, Project administration, Supervision, Writing - original draft, Writing - review & editing. **Yimin Deng:** Data curation, Formal analysis, Investigation, Writing - review & editing. **Xianlu Wang:** Validation, Writing - review & editing. **Huili Zhang:** Funding acquisition, Project administration, Resources, Supervision, Writing - original draft, Writing - review & editing.

## Acknowledgements

We gratefully acknowledge the support by National Key Research and Development Project [No. 2018YFE0107400] from Ministry of Science and Technology of the People's Republic of China, China; by the Fundamental Research Fund for the Central Universities [No. buctrc201726] from Beijing University of Chemical Technology, China; and by Beijing Advanced Innovation Center for Soft Matter Science and Engineering of the Beijing University of Chemical Technology, China.

## Appendix A. Supplementary data

Supplementary data to this article can be found online at https://doi.org/10.1016/j.jenvman.2020.110582.

## Declaration of interests

The authors declare that they have no known competing financial interests or personal relationships that could have appeared to influence the work reported in this paper.

## References


Agrafiotis, C., Block, T., Senholdt, M., Tescari, S., Roeb, M., Sattler, C., 2017. Exploitation of thermochemical cycles based on solid oxide redox systems for thermochemical storage of solar heat. Part 6: testing of Mn-based combined oxides and porous structures. Sol. Energy 149, 227–244. https://doi.org/10.1016/j.solener.2017.03.083.

Agrafiotis, C., Roeb, M., Schmücker, M., Sattler, C., 2015a. Exploitation of thermochemical cycles based on solid oxide redox systems for thermochemical storage of solar heat. Part 2: redox oxide-coated porous ceramic structures as integrated thermochemical reactors/heat exchangers. Sol. Energy 114, 440–458. https://doi.org/10.1016/j.solener.2014.12.036.

Agrafiotis, C., Tescari, S., Roeb, M., Schmücker, M., Sattler, C., 2015b. Exploitation of thermochemical cycles based on solid oxide redox systems for thermochemical storage of solar heat. Part 3: cobalt oxide monolithic porous structures as integrated thermochemical reactors/heat exchangers. Sol. Energy 114, 459–475. https://doi.org/10.1016/J.SOLENER.2014.12.037.

Al-Shankiti, I.A., Ehrhart, B.D., Ward, B.J., Bayon, A., Wallace, M.A., Bader, R., et al., 2019. Particle design and oxidation kinetics of iron-manganese oxide redox materials for thermochemical energy storage. Sol. Energy 183, 17–29. https://doi.org/10.1016/j.solener.2019.02.071.

Alonso, E., Gallo, A., Pérez-Rábago, C., Fuentealba, E., 2016. Thermodynamic study of CuO/$Cu_2O$ and $Co_3O_4$/CoO redox pairs for solar energy thermochemical storage. AIP Conf. Proc. 1734 https://doi.org/10.1063/1.4949102.

André, L., Abanades, S., 2017. Evaluation and performances comparison of calcium, strontium and barium carbonates during calcination/carbonation reactions for solar thermochemical energy storage. J. Energy Storage 13, 193–205. https://doi.org/10.1016/j.est.2017.07.014.

André, L., Abanades, S., Cassayre, L., 2017. High-temperature thermochemical energy storage based on redox reactions using Co-Fe and Mn-Fe mixed metal oxides. J. Solid State Chem. 253, 6–14. https://doi.org/10.1016/J.JSSC.2017.05.015.

Angerer, M., Becker, M., Härzschel, S., Kröper, K., Gleis, S., Vandersickel, A., Spliethoff, H., 2018. Design of a MW-scale thermo-chemical energy storage reactor. Energy Rep. 4, 507–519. https://doi.org/10.1016/J.EGYR.2018.07.005.

AuYeung, N., Kreider, P., 2017. Solar thermochemical energy storage. Chem. Eng. Prog. 113.

Bielsa, D., Zaki, A., Faik, A., Arias, P.L., 2019. Efficiency improvement of $Mn_2O_3$/$Mn_3O_4$ redox reaction by means of different operation strategies. SOLARPACES 2018 Int. Conf. Conc. Sol. Power Chem. Energy Syst. 2126, 210001. https://doi.org/10.1063/1.5117750.

Block, T., Knoblauch, N., Schmücker, M., 2014. The cobalt-oxide/iron-oxide binary system for use as high temperature thermochemical energy storage material. Thermochim. Acta 577, 25–32. https://doi.org/10.1016/J.TCA.2013.11.025.

Block, T., Schmücker, M., 2016. Metal oxides for thermochemical energy storage: a comparison of several metal oxide systems. Sol. Energy 126, 195–207. https://doi.org/10.1016/J.SOLENER.2015.12.032.

Brems, A., Baeyens, J., Beerlandt, J., Dewil, R., 2011. Thermogravimetric pyrolysis of waste polyethylene-terephthalate and polystyrene : a critical assessment of kinetics modelling. Resour. Conserv. Recycl. 55, 772–781. https://doi.org/10.1016/j.resconrec.2011.03.003.

Carrillo, A.J., Serrano, D.P., Pizarro, P., Coronado, J.M., 2016. Understanding redox kinetics of iron-doped manganese oxides for high temperature thermochemical energy storage. J. Phys. Chem. C 120, 27800–27812. https://doi.org/10.1021/acs.jpcc.6b08708.

Carrillo, A.J., Serrano, D.P., Pizarro, P., Coronado, J.M., 2015. Thermochemical heat storage at high temperatures using $Mn_2O_3$/$Mn_3O_4$ system: narrowing the redox hysteresis by metal co-doping. Energy Procedia 73, 263–271. https://doi.org/10.1016/J.EGYPRO.2015.07.686.

Chase J., M.W., 1988. NIST-JANAF themochemical tables. fourth ed. J. Phys. Chem. Ref. Data. Monogr. 9, American Chemical Society, Washington DC and American Institute of Physics for the National Institute of Standards and Technology, Woodbury.

Criado, Y.A., Huille, A., Rougé, S., Abanades, J.C., 2017. Experimental investigation and model validation of a CaO/$Ca(OH)_2$ fluidized bed reactor for thermochemical energy storage applications. Chem. Eng. J. 313, 1194–1205. https://doi.org/10.1016/j.cej.2016.11.010.

Farcot, L., Le Pierrès, N., Michel, B., Fourmigué, J.F., Papillon, P., 2018. Numerical investigations of a continuous thermochemical heat storage reactor. J. Energy Storage 20, 109–119. https://doi.org/10.1016/j.est.2018.08.020.

Fernandes, D., Pitié, F., Cáceres, G., Baeyens, J., 2012. Thermal energy storage: "How previous findings determine current research priorities. Energy 39, 246–257. https://doi.org/10.1016/J.ENERGY.2012.01.024.

Fernandez, A., Soria, J., Rodriguez, R., Baeyens, J., Mazza, G., 2019. Macro-TGA steam-assisted gasification of lignocellulosic wastes. J. Environ. Manag. 233, 626–635. https://doi.org/10.1016/j.jenvman.2018.12.087.

Fopah-Lele, A., Rohde, C., Neumann, K., Tietjen, T., Rönnebeck, T., N'Tsoukpoe, K.E., et al., 2016. Lab-scale experiment of a closed thermochemical heat storage system including honeycomb heat exchanger. Energy 114, 225–238. https://doi.org/10.1016/j.energy.2016.08.009.

Gokon, N., Nishizawa, A., Yawata, T., Bellan, S., Kodama, T., Cho, H.-S., 2019. Fe-doped manganese oxide redox material for thermochemical energy storage at high-temperatures. SOLARPACES 2018 Int. Conf. Conc. Sol. Power Chem. Energy Syst. 2126, 210003. https://doi.org/10.1063/1.5117752.

Hawwash, A.A., Hassan, H., Ahmed, M., Ookawara, S., Feky, K. El, 2017. Long-term thermal energy storage using thermochemical materials. Energy Procedia 141, 310–314. https://doi.org/10.1016/j.egypro.2017.11.111.

Kang, Q., Dewil, R., Degrève, J., Baeyens, J., Zhang, H., 2018. Energy analysis of a particle suspension solar combined cycle power plant. Energy Convers. Manag. 163, 292–303.

Lei, Q., Bader, R., Kreider, P., Lovegrove, K., Lipiński, W., 2017. Thermodynamic analysis of a combined-cycle solar thermal power plant with manganese oxide-based thermochemical energy storage. E3S Web Conf 22. https://doi.org/10.1051/e3sconf/20172200102.

Li, S., Kong, W., Zhang, H., Sabatier, F., Ansart, R., Flamant, G., Baeyens, J., 2019. The fluidized bed air heat exchanger in a hybrid Brayton-cycle solar power plant. SOLARPACES 2018 Int. Conf. Conc. Sol. Power Chem. Energy Syst. 2126, 140002. https://doi.org/10.1063/1.5117650.

Li, S., Liu, J., Tan, T., Nie, J., Zhang, H., 2020. Optimization of $LiNO_3$–$Mg(OH)_2$ composites as thermo-chemical energy storage materials. J. Environ. Manag. 262, 110258. https://doi.org/10.1016/j.jenvman.2020.110258.

Liu, J., Baeyens, J., Deng, Y., Tan, T., Zhang, H., 2020. The chemical $CO_2$ capture by carbonation-decarbonation cycles. J. Environ. Manag. 260 https://doi.org/10.1016/j.jenvman.2019.110054.

Liu, J., Wang, N., Zhang, H., Baeyens, J., 2019. Adsorption of Congo red dye on $Fe_xCo_{3-x}O_4$ nanoparticles. J. Environ. Manag. 238, 473–483. https://doi.org/10.1016/j.jenvman.2019.03.009.

Mahmoudi, S., Chan, C.W., Brems, A., Seville, J., Baeyens, J., 2012. Solids flow diagram of a CFB riser using Geldart B-type powders. Particuology 10, 51–61. https://doi.org/10.1016/j.partic.2011.09.002.

Naish, C., McCubbin, I., Edberg, O., Harfoot, M., 2008. Outlook of Energy Storage Technologies. Rep. to Eur. Parliam.. http://www.europarl.europa.eu/document/.

Pagkoura, C., Karagiannakis, G., Zygogianni, A., Lorentzou, S., Konstandopoulos, A.G., 2015. Cobalt oxide based honeycombs as reactors/heat exchangers for redox thermochemical heat storage in future CSP plants. Energy Procedia 69, 978–987. https://doi.org/10.1016/j.egypro.2015.03.183.

Pan, Z.H., Zhao, C.Y., 2017. Gas–solid thermochemical heat storage reactors for high-temperature applications. Energy 130, 155–173. https://doi.org/10.1016/j.energy.2017.04.102.

Peng, X., Root, T.W., Maravelias, C.T., 2017. Storing solar energy with chemistry: the role of thermochemical storage in concentrating solar power. Green Chem. 19, 2427–2438. https://doi.org/10.1039/c7gc00023e.

Ranjha, Q.A., Vahedi, N., Oztekin, A., 2017. High temperature thermochemical energy storage using packed beds. Proc. ASME 2016 Int. Mech. Eng. Congr. Expo. 11–17.

Rougé, S., Criado, Y.A., Soriano, O., Abanades, J.C., 2017. Continuous CaO/$Ca(OH)_2$ fluidized bed reactor for energy storage: first experimental results and reactor model validation. Ind. Eng. Chem. Res. 56, 844–852. https://doi.org/10.1021/acs.iecr.6b04105.

Sabatier, F., Ansart, R., Zhang, H., Baeyens, J., Simonin, O., 2020. Experiments support simulations by the NEPTUNE_CFD code in an upflow bubbling fluidized bed reactor. Chem. Eng. J. 385 https://doi.org/10.1016/j.cej.2019.123568.

Schildermans, I., Baeyens, J., Smolders, K., 2004. Pulse jet cleaning of rigid filters: a literature review and introduction to process modelling. Filtr. Sep. 41, 26–33. https://doi.org/10.1016/S0015-1882(04)00234-4.

Schmidt, M., Gollsch, M., Giger, F., Grün, M., Linder, M., 2016. Development of a moving bed pilot plant for thermochemical energy storage with CaO/$Ca(OH)_2$. AIP Conf. Proc. 1734 https://doi.org/10.1063/1.4949139.

Silakhori, M., Jafarian, M., Arjomandi, M., Nathan, G.J., 2019. Thermogravimetric analysis of Cu, Mn, Co, and Pb oxides for thermochemical energy storage. J. Energy Storage 23, 138–147. https://doi.org/10.1016/j.est.2019.03.008.

Smolders, K., Baeyens, J., 2000. Cleaning of Hot Calciner Exhaust Gas by Low-Density Ceramic Filters 240–244.

Smolders, K., Baeyens, J., 1995. The operation of L-valves to control standpipe flow. Adv. Powder Technol. 6, 163–176. https://doi.org/10.1016/S0921-8831(08)60525-7.

Tescari, S., Agrafiotis, C., Breuer, S., de Oliveira, L., Puttkamer, M.N., Roeb, M., Sattler, C., 2014. Thermochemical solar energy storage via redox oxides: materials and reactor/heat exchanger concepts. Energy Procedia 49, 1034–1043. https://doi.org/10.1016/j.egypro.2014.03.111.

Tregambi, C., Montagnaro, F., Salatino, P., Solimene, R., 2017. Directly irradiated fluidized bed reactors for thermochemical processing and energy storage: application to calcium looping. AIP Conf. Proc. 1850 https://doi.org/10.1063/1.4984456.

Van de Velden, M., Baeyens, J., 2007. Attrition and erosion in particle transport loops. Powder Handling Process. 19, 29–33.

Van de Velden, M., Baeyens, J., Brems, A., Janssens, B., Dewil, R., 2010. Fundamentals, kinetics and endothermicity of the biomass pyrolysis reaction. Renew. Energy 35, 232–242. https://doi.org/10.1016/j.renene.2009.04.019.

Wei, J., Feng, Y., Liu, Y., Ding, Y., 2015. $M_xCo_{3-x}O_4$ (M=Co, Mn, Fe) porous nanocages derived from metal–organic frameworks as efficient water oxidation catalysts. J. Mater. Chem. 3, 22300–22310. https://doi.org/10.1039/C5TA06411B.

Wokon, M., Block, T., Nicolai, S., Linder, M., Schmücker, M., 2017a. Thermodynamic and kinetic investigation of a technical grade manganese-iron binary oxide for thermochemical energy storage. Sol. Energy 153, 471–485. https://doi.org/10.1016/j.solener.2017.05.045.

Wokon, M., Kohzer, A., Linder, M., 2017b. Investigations on thermochemical energy storage based on technical grade manganese-iron oxide in a lab-scale packed bed reactor. Sol. Energy 153, 200–214. https://doi.org/10.1016/j.solener.2017.05.034.

Zhang, H., Baeyens, J., Cáceres, G., Degrève, J., Lv, Y., 2016a. Thermal energy storage: recent developments and practical aspects. Prog. Energy Combust. Sci. 53, 1–40. https://doi.org/10.1016/j.pecs.2015.10.003.

Zhang, H., Degrève, J., Baeyens, J., Wu, S.-Y., 2016b. Powder attrition in gas fluidized beds. Powder Technol. 287, 1–11. https://doi.org/10.1016/j.powtec.2015.08.052.

Zhang, H., Gowing, T., Degrève, J., Leadbeater, T., Baeyens, J., 2016c. Use of particle heat carriers in the stirling engine concept. Energy Technol. 4, 401–408. https://doi.org/10.1002/ente.201500274.

Zhang, H., Huys, K., Baeyens, J., Degrève, J., Kong, W., Lv, Y., 2016d. Thermochemical energy storage for power generation on demand. Energy Technol. 4, 341–352. https://doi.org/10.1002/ente.201500261.

Zhang, H., Kong, W., Tan, T., Baeyens, J., 2017. High-efficiency concentrated solar power plants need appropriate materials for high-temperature heat capture, conveying and storage. Energy 139, 52–64. https://doi.org/10.1016/j.energy.2017.07.129.

Zhang, H., Li, S., Kong, W., Flamant, G., Baeyens, J., 2019. Scale-up considerations of the UBFB solar receiver. SOLARPACES 2018 Int. Conf. Conc. Sol. Power Chem. Energy Syst. 2126, 030067 https://doi.org/10.1063/1.5117579.

Zhou, T., Liu, W., Peng, T., 2013. A Kind of Preparation Method of Manganese Trioxide Micropowder and the Application, CN103700830A.